Bulletin of the Seismological Society of America, Vol. 103, No. 2B, pp. 1275–1289, May 2013, doi: 10.1785/0120120136

Ⓔ

Rupture to the Trench: Dynamic Rupture Simulations of the 11 March 2011 Tohoku Earthquake

by Jeremy E. Kozdon* and Eric M. Dunham

Abstract There is strong evidence that the 11 March 2011 Tohoku earthquake rupture reached the seafloor. This is surprising because the shallow portion of the plate interface in subduction zones is thought to be frictionally stable, leading to the widely held view that coseismic rupture would stop several tens of kilometers downdip of the seafloor. Various explanations have been proposed to reconcile this seeming inconsistency, including dynamic weakening (e.g., thermal pressurization) and extreme stress release around shallow subducted seamounts. We offer a simpler explanation supported by 2D dynamic rupture simulations of the Tohoku earthquake. Our models account for depth-dependent material properties and the complex geometry of the fault, seafloor, and material interfaces, based on seismic surveys of the Japan Trench. The fault obeys rate-and-state friction with standard logarithmic dependence of shear strength on slip velocity in steady state. In our preferred model, the uppermost section of the fault is velocity strengthening. Rupture nucleates on a deeper, velocity-weakening section. Waves released by deep slip reflect off the seafloor, transmitting large stress changes to the upper section of the fault driving the rupture through the velocity-strengthening region to the trench. We validate the model against seafloor deformation and 1-Hz Global Positioning System (GPS) data. The seafloor displacements constrain the seismogenic depth and overall amount of slip, particularly near the trench. Our simulations reproduce many features in the GPS data, thereby providing insight into the rupture process and seismic wave field. Sensitivity to parameters is explored through an extensive suite of simulations. Neither static seafloor deformation nor onshore 1-Hz GPS data can uniquely determine near-trench frictional properties due to trade-offs with average stress drop. While conducted specifically for the Japan Trench region, our simulations suggest that rupture to the trench in megathrust events is quite possible, even if velocity-strengthening properties extend tens of kilometers landward from the trench.

Online Material: Mp4 movies of particle velocities.

Introduction

Over the past several decades, studies of subduction zones have led to the widely accepted premise that the seismogenic zone (i.e., the region that slips coseismically in megathrust ruptures) begins several tens of kilometers downdip of the trench axis and extends downward another 100–200 km. Beyond the lower limit, located at a depth of 30–50 km, relative motion across the plate interface occurs as stable sliding at the plate convergence rate. This aseismic portion of the fault is frequently connected to the seismogenic zone through a transitional region exhibiting slow slip events and seismic tremor. Byrne *et al.* (1988), Hyndman *et al.* (1997), Moore and Saffer (2001), and many others have suggested that the seismogenic zone does not extend all the way to the trench axis, but instead terminates at 5–10 km depth, with the shallower portion of the fault beneath the accretionary prism accommodating deformation aseismically. Supporting evidence includes the lack of shallow seismicity near the trench axis (Byrne *et al.*, 1988), which has been explained by the stable frictional properties of underconsolidated clay-rich sediments along the plate interface in this region (Marone and Scholtz, 1988; Vrolijk, 1990; Saffer and Marone, 2003; Ikari *et al.*, 2009; den Hartog *et al.*, 2012). For a more complete discussion of subduction zone mechanics, see Saffer and Tobin (2011).

Frictional stability is typically discussed in the context of rate-and-state friction. In the absence of extreme dynamic

*Now at Department of Applied Mathematics, Naval Postgraduate School, 833 Dyer Road, Monterey, California 93943.

weakening, the steady-state friction coefficient depends on slip velocity V as

$$f_{ss}(V) = f_0 - (b-a)\ln(V/V_0), \tag{1}$$

in which f_0 is the friction coefficient for steady sliding at reference velocity V_0, and the sign of $b-a$ determines if frictional strength decreases ($b-a>0$, velocity weakening) or increases ($b-a<0$, velocity strengthening) with increasing slip velocity. Unstable slip and earthquake nucleation can only occur on faults with velocity-weakening friction.

The M_w 9.0 Tohoku earthquake challenges the conventional view of subduction megathrust events summarized previously. A wide range of observational evidence (Fujiwara *et al.*, 2011; Ide *et al.*, 2011; Ito *et al.*, 2011; Kido *et al.*, 2011; Sato *et al.*, 2011; Kodaira *et al.*, 2012) indicates that coseismic rupture extended all the way to the seafloor, with ~20–40 m slip occurring near the trench axis. This came as a surprise to many, given that the depth dependence of seismicity in the Japan Trench is quite consistent with the presence of velocity-strengthening frictional properties along the upper part of the plate interface. Based on an early earthquake catalog for this region, Byrne *et al.* (1988) suggested that the upper limit of the seismogenic zone lies 45 km landward of the trench axis.

Without consideration of megathrust rupture dynamics, it appears difficult to reconcile the immense coseismic shallow slip observed in the Tohoku earthquake with the likely presence of velocity-strengthening properties along the uppermost portion of the plate interface. This has led some authors (Kennett *et al.*, 2011; Matsubara and Obara, 2011; Duan, 2012) to speculate about the existence of subducted seamounts that enhanced plate coupling, leading to strain accumulation around the trench. Others (Shibazaki *et al.*, 2011) have suggested, based on laboratory experiments (Ujiie and Tsutsumi, 2010; Faulkner *et al.*, 2011), that the fault response switches from velocity strengthening at low slip rates to velocity weakening at high slip rates. In this way, while the shallow portion of the fault is incapable of nucleating earthquakes, it is quite capable of slipping coseismically as part of a larger rupture initiated at depth. Similar arguments have been made invoking thermal pressurization of pore fluids and other dynamic weakening mechanisms that are activated only at sufficiently high slip rates (Noda and Lapusta, 2011; Mitsui *et al.*, 2012).

Although we do not argue against any of the previously presented ideas, consideration of rupture dynamics suggests a much simpler explanation. Ruptures indeed must nucleate on velocity-weakening parts of the fault, but they do not stop abruptly when entering velocity-strengthening regions, as has implicitly been assumed in most discussions regarding the extent of the seismogenic zone. This suggests that unstable deep slip might, in fact, drive the upper portion of the fault to slip coseismically, regardless of its frictional properties. In the shallowly dipping subduction geometry, free-surface interactions further facilitate shallow slip near the seafloor. In this study, we present dynamic rupture models of the Tohoku event that demonstrate the ease with which megathrust ruptures, nucleated within a velocity-weakening region at depth, penetrate through shallow velocity-strengthening regions several tens of kilometers long with little diminution of slip.

Rupture Penetration into Velocity-Strengthening Regions

The ability of a rupture to penetrate a significant distance into a velocity-strengthening region can be illustrated with the following simple example. We assume that fault strength degrades rapidly to a nearly constant residual strength behind the propagating rupture, permitting us to use the idealizations of linear elastic fracture mechanics. The rupture front advances at a speed determined by balancing the energy release rate, G, with the fracture energy, Γ. For subshear propagation of a mode II rupture along a planar interface between identical elastic half-spaces,

$$G = G_0 g(v_r), \qquad G_0 = \frac{K_0^2}{2\mu/(1-\nu)}, \tag{2}$$

where G_0 and K_0 are the energy release rate and stress intensity factor, respectively, at vanishingly small rupture velocity v_r; μ is shear modulus; ν is Poisson's ratio; and $g(v_r)\approx 1 - v_r/c_R$, where c_R is the Rayleigh wave speed (Fossum and Freund, 1975). The equation of motion, $G=\Gamma$, thus shows that the rupture advances only when $G_0 > \Gamma$.

The stress concentration at the crack tip depends on the history of stress drop $\Delta\tau$ along the ruptured portion of the interface. For a semi-infinite crack advancing along the x axis with its tip at $x=\ell(t)$ (Fossum and Freund, 1975),

$$K_0 = \sqrt{\frac{2}{\pi}}\int_{-\infty}^{\ell(t)} \frac{\Delta\tau(x)}{\sqrt{\ell(t)-x}}\,dx. \tag{3}$$

A crude model of a finite-length crack $0<x<\ell(t)$ is obtained by setting $\Delta\tau = 0$ for $x<0$, though that underestimates the stiffness of the system by permitting free slip along the $x<0$ section of the interface. A similar approximation for mode III cracks was discussed by Eshelby (1969).

This model can be applied to faults obeying rate-and-state friction. We can estimate the stress drop by choosing the reference velocity V_0 such that the prestress (assumed to be everywhere identical) is $f_0\bar{\sigma}$, where $\bar{\sigma}$ is the (assumed constant) effective normal stress. Then the stress drop is $\Delta\tau = (b-a)\bar{\sigma}\ln(V/V_0)$, where V is a typical coseismic slip rate (~1 m/s).

Consider a rupture that begins in a velocity-weakening region $0<x<\ell_0$ with constant stress drop $\Delta\tau_1>0$, followed by a velocity-strengthening region $x>\ell_0$ with constant stress drop $\Delta\tau_2<0$ (Fig. 1). How far into the velocity-strengthening region will the rupture penetrate?

From (2) and (3), the static energy release rate G_0 increases linearly with propagation distance in the velocity-weakening region. Upon entering the velocity-strengthening region, G_0 begins to decrease and eventually drops to Γ,

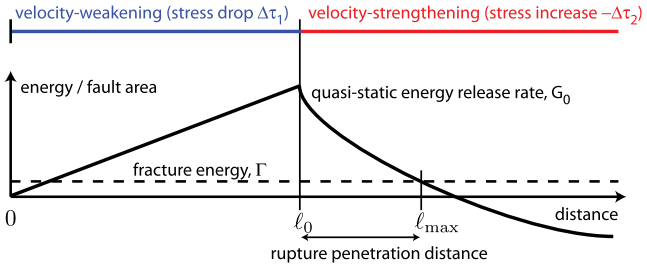

Figure 1. Linear elastic fracture mechanics calculation of rupture growth into a velocity-strengthening region. Propagation occurs where $G_0 > \Gamma$. The color version of this figure is available only in the electronic edition.

whereupon the rupture arrests at $x = \ell_{max}$ (Fig. 1). We can obtain an upper bound on the penetration distance, $\ell_{max} - \ell_0$, by neglecting the fracture energy and solving for the crack tip position at which K_0 (and, thus, G_0) vanishes. The resulting penetration distance is

$$\ell_{max} - \ell_0 = \frac{\ell_0}{(1+T)^2 - 1}, \tag{4}$$

where $T \equiv (-\Delta\tau_2)/\Delta\tau_1$. For example, if the stress increase in the velocity-strengthening region equals the stress decrease in the velocity-weakening region (i.e., $T = 1$), then the rupture penetrates a distance $\ell_0/3$ into the velocity-strengthening region.

For subduction zones with velocity-weakening regions having along-dip extents of 100–200 km, the predicted penetration distance is several tens of kilometers. The estimate presented in (4) neglects fracture energy, which will arrest ruptures sooner. Counteracting this, however, are reductions in normal stress that occur as a rupture approaches the free surface (Dmowska and Kostrov, 1973; Dmowska and Rice 1986). These facilitate unstable shallow slip (Rudnicki and Wu, 1995). Perhaps even more important at the low-dip angles in many subduction zones are shear stress changes carried by wave reflections from the surface. These could potentially lead to dynamic overshoot of the stress concentration above its quasi-static value. Quantifying these effects, as well as the role of variable material properties, fault nonplanarity, and the finiteness of the crack, requires dynamic rupture modeling.

Dynamic Rupture Model

Our objective is to use dynamic rupture models of the Tohoku earthquake to identify conditions that permit slip to the trench. The earthquake extended over 500 km along strike and about 200 km along dip. Propagation up- and downdip dominated the rupture process for the first 100 s or so, followed by along-strike spreading of the rupture. These features justify the use of a 2D plane strain model that assumes invariance of fields along strike, with the understanding that we are neglecting the later along-strike expansion phase.

In this study, we assume the medium is an isotropic, linear elastic solid with piecewise constant material properties (density ρ and P- and S-wave speeds c_p and c_s, respectively). The specific geometry and material structure (Fig. 2 and Table 1) are based on Miura *et al.* (2001, 2005), but with average properties assigned to each of the material blocks. Those studies reported P-wave velocity and density, and we assume Poisson's ratio of 1/4, for which $c_p = \sqrt{3}c_s$. The plate interface, shown in Figure 2 as the thicker solid line, is curved and in many places lies at the boundary between different elastic materials. Bimaterial effects must therefore be considered. We do not explicitly include the accretionary prism in the material structure, but do account for different frictional properties along this uppermost section of the fault.

We take the seafloor to be a free surface that constitutes the upper boundary of the simulation domain. Later in the paper, we justify this assumption by adding a water layer

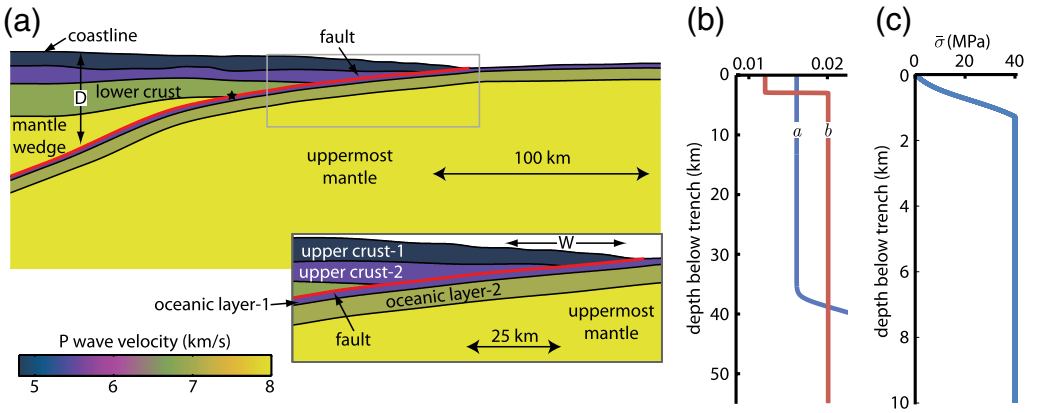

Figure 2. (a) P-wave velocity structure for the dynamic rupture simulations (no vertical exaggeration). The geometry and piecewise constant material properties are derived from Miura *et al.* (2001, 2005). The velocity-weakening region ($b - a > 0$) starts updip at horizontal distance W from the trench and ends downdip at depth D below sea level. The nucleation location for all simulations is indicated with the black star. The inset shows the velocity structure near the trench axis, where the dip angle is 6° from horizontal and 7° from the seafloor. (b) Depth dependence of friction parameters a and b for $W = 30$ km and $D = 45$ km. (c) Depth dependence of effective normal stress $\bar{\sigma}$ for $\bar{\sigma}_{max} = 40$ MPa. The color version of this figure is available only in the electronic edition.

(modeled as an isotropic acoustic medium) to the model to demonstrate that this has a negligible effect on the rupture process. Nonreflecting boundary conditions based on characteristic variables (Kozdon *et al.*, 2012) are used on the remaining three sides (Fig. 2 shows only 2%–3% of the domain, and the outer boundaries are distant enough that boundary effects do not influence the rupture process).

Fault slip occurs along the plate interface, which is governed by rate-and-state friction. In the standard formulation, fault shear strength τ is directly proportional to the effective normal stress $\bar{\sigma} = \sigma - p$, the difference between total normal stress σ and pore pressure p. Both σ and $\bar{\sigma}$ are positive in compression. Abrupt changes in $\bar{\sigma}$ cause similarly abrupt changes in τ. For sliding between dissimilar elastic solids, this instantaneous coupling of shear and effective normal stress can lead to instability and ill posedness (Cochard and Rice, 2000; Ranjith and Rice, 2001; Rice *et al.*, 2001).

To alleviate this problem, we instead consider a friction law in a differential form:

$$\frac{d\tau}{dt} = \frac{a\bar{\sigma}}{V}\tanh\left(\frac{\tau}{a\bar{\sigma}}\right)\frac{dV}{dt} - \frac{V}{L}[|\tau| - \bar{\sigma} f_{ss}(V)], \qquad (5)$$

where the steady-state friction coefficient is given by (1). For constant $\bar{\sigma}$, equation (5) is equivalent to the regularized rate-and-state law used by Lapusta *et al.* (2000) with slip-law state evolution and is valid even when $V = 0$ (as well as for both positive and negative V and τ). This correspondence ceases when $\bar{\sigma}$ is not constant in time, as will be the case in our simulations because of fault nonplanarity, bimaterial effects, and free-surface interactions. As is evident from (5), changes in $\bar{\sigma}$ lead to changes in τ only with sufficient slip, as observed in experiments (Prakash and Clifton, 1993; Prakash, 1998).

We explicitly consider undrained poroelastic alterations of pore pressure, Δp, in response to changes in total normal stress, $\Delta\sigma$. We assume a linear relation of the form $\Delta p = B\Delta\sigma$, where $0 \le B < 1$. Cocco and Rice (2002) have shown that for faults bounded by highly damaged material, B can be identified as Skempton's coefficient (Rice and Cleary, 1976; Wang, 2000) of the fault material. Rudnicki and Rice (2006) and Dunham and Rice (2008) have developed a more comprehensive poroelastic fault-zone model that accounts for short-time-scale fluid diffusion across the slip surface and its resulting effect on fault pore pressure, but that model introduces several other parameters that cannot be constrained with any accuracy. The simple model we adopt provides a buffering effect on effective stress. Writing the total normal stress as the sum of an initial value and a perturbation caused by fault slip, $\sigma = \sigma_0 + \Delta\sigma$, the effective normal stress is

$$\bar{\sigma} = \bar{\sigma}_0 + (1 - B)\Delta\sigma. \qquad (6)$$

In the $B \to 1$ limit, effective stress on the fault remains constant. We assume a more moderate value of $B = 0.6$ over the entire fault in all simulations.

In the following paragraphs, we describe the selection of model parameters (friction, stress, etc.). Through trial-and-error forward modeling and comparison with data, we have identified a preferred model. The parameters of that model are referred to as the nominal parameters; in the latter part of this paper, we present an extensive set of simulations that explore how the model results change as we vary parameters about their nominal values.

Because we assume ideally elastic off-fault material response, initial stresses and pore pressure need only be specified on the fault. In the shallowest sections of the fault, we assume that total normal stress is lithostatic and pore pressure is hydrostatic (with a water density of 1000 kg/m^3), such that effective normal stress increases linearly with depth for constant rock density. Following Rice (1992), we assume that below some depth, the pore pressure departs from its hydrostatic trend and begins to track the lithostatic gradient, yielding a depth-independent maximum effective stress $\bar{\sigma}_{\max}$. Because $\bar{\sigma}_{\max}$ is so poorly constrained, we treat it as a model parameter with a nominal value of 40 MPa. The effective normal stress profile we adopt is shown in Figure 2c. The initial shear stress on the fault is $\tau_0 = 0.6\bar{\sigma}_0$, and the initial slip velocity of the fault is $V_{ini} = 1$ μm/s. The latter is equivalent to specifying an initial state variable with the usual rate-and-state friction law, and it is chosen to provide a reasonable static friction coefficient of approximately 0.6.

We next discuss the depth dependence of frictional properties. The state-evolution distance L and the reference friction coefficient and slip velocity, f_0 and V_0, are constant across all simulations and independent of depth (see Table 2). The central velocity-weakening portion of the plate interface (nominally located at depths between 2.8 km and 37.3 km below the trench axis) has $b - a = 0.004$. Starting at the downdip limit of the seismogenic zone (specified here in terms of the depth D below sea level; see Fig. 2), we linearly increase the direct-effect parameter a with depth so that $b - a$ becomes negative, and rupture will cease after penetrating some small distance into this velocity-strengthening region.

Table 1
Material Parameters*

Layer Name	*P*-Wave Velocity (km/s)	*S*-Wave Velocity (km/s)	Density (kg/m^3)	Shear Modulus (GPa)
Upper crust-1	4.8	2.8	2200	16.9
Upper crust-2	5.5	3.2	2600	26.2
Lower crust	7.0	4.0	2800	45.7
Mantle wedge	8.0	4.6	3200	68.3
Oceanic layer-3	5.5	3.2	2600	26.2
Oceanic layer-2	6.8	3.9	2800	43.1
Uppermost mantle	8.0	4.6	3200	68.3
Water†	1.5	0	1000	0

*For layers, see Figure 2.
†Water layer is included in only one simulation.

We nominally choose $D = 45$ km (corresponding to 11.6 km offshore and 37.3 km below the trench axis), though other depths will be considered as part of this work. For computational reasons, it is typical for state-evolution distance L to be chosen based on the global scale of the problem rather than laboratory experiments. Our choice of $L = 0.8$ m reflects this as it is several orders of magnitude larger than values inferred from laboratory experiments.

We also account for a change in frictional properties along the shallowest portion of the plate interface beneath the accretionary prism. This uppermost region has a horizontal extent W (see Fig. 2), which we nominally take as $W =$ 30 km (corresponding to 2.8 km depth below the trench axis), based on the location of the accretionary prism in the seismic velocity structure of Miura *et al.* (2001, 2005). We also explore other values of W as part of this study. We consider three different cases for frictional properties beneath the accretionary prism: $b - a = 0.004$ (velocity weakening), $b - a = 0$ (neutrally stable), and $b - a = -0.004$ (velocity strengthening). The transition from the deeper velocity-weakening parameters is accomplished by increasing the state-evolution parameter b over a 1 km transition length (5 grid points). Figure 2b illustrates this for the shallow velocity-strengthening case with nominal parameters $W = 30$ km and $D = 45$ km.

To nucleate the earthquake we apply a time-dependent shear stress perturbation centered on $(x_0, y_0) = (-109.6$ km, -13.1 km) relative to the trench axis (relative to the coastline, this is 82.3 km offshore at a depth of 20.8 km below sea level). This nucleation location is in the lower crust and 100 m above the mantle wedge. This choice of hypocenter was chosen to reproduce the duration of rupture between the initial onset of rapid propagation and breakout at the trench, as well as onshore displacement waveforms recorded by 1-Hz Global Positioning System (GPS) stations. The perturbation is Gaussian in space with width (standard deviation) of (75 MPa/$\bar{\sigma}_{\max}$) km, and the amplitude increases in time according to $0.5\bar{\sigma}_{\max}[1 - \exp(-t/10^{-2}\text{ s})]$. This abrupt nucleation procedure, which leads to immediate propagation at a healthy fraction of the S-wave speed, is not intended to be realistic. In fact, we later see that this procedure introduces features in synthetic seismograms that are not seen in actual onshore 1-Hz GPS data. Because nucleation occurs sufficiently deep, this procedure does not influence any of our conclusions regarding the ability of the rupture to reach the trench, which is the primary focus of this study.

Table 2
Frictional Properties

Parameter	Symbol	Value
Direct-effect parameter	a	Variable
Evolution-effect parameter	b	Variable
Reference slip velocity	V_0	1 μm/s
Steady-state friction coefficient at V_0	f_0	0.6
State evolution distance	L	0.8 m
Initial slip velocity	V_{ini}	1 μm/s
Initial effective normal stress on fault	$\bar{\sigma}_0$	Variable
Initial shear stress on fault	τ_0	$0.6\bar{\sigma}_0$

Computationally, we simultaneously solve the elastic wave equation and the rate-and-state friction law using the high-order finite-difference method developed by Kozdon *et al.* (2012). The method handles frictional sliding in a provably stable and accurate manner, as evidenced through rigorous convergence tests. Complex geometries are handled with multiblock grids and coordinate transforms. The underlying numerical method is based on summation-by-parts finite-difference operators (Kreiss and Scherer, 1974; Strand, 1994) and weak enforcement of boundary/interface conditions through the use of the simultaneous approximation term method (Carpenter *et al.*, 1994).

The numerical model we construct for this simulation consists of 1.1×10^7 grid points, with a typical grid spacing on the fault of 200 m. After ~500 km horizontal distance from the fault and 100 km depth, we use a grid-stretching technique to place the outer boundaries sufficiently far from the region of interest that numerical reflections have negligible influence on the rupture process.

Dynamic Rupture Process

We begin by presenting our preferred dynamic rupture simulation with a focus on the rupture history, seismic wave field, and displacements. In this model, the near-trench region has velocity-strengthening friction ($b - a = -0.004$) over a horizontal extent of $W = 30$ km, and the lower limit of the seismogenic zone is at a depth of $D = 45$ km. The maximum background effective normal stress is $\bar{\sigma}_{\max} =$ 40 MPa. In all simulation results and plots, time $t = 0$ corresponds to the start of the artificial nucleation process. To account for the more gradual onset of the actual event, we allow for a time shift in 1-Hz GPS data and inferred moment rate functions when comparing with our simulations.

Figure 3 shows snapshots of cumulative slip, which reaches a peak value of 26 m at the trench despite the fault being velocity-strengthening in this region. Because our plane strain model effectively extends the slip distribution indefinitely far along strike, our predicted values of slip must be viewed as lower bounds. In other words, it might be necessary to increase slip in a 3D model of limited along-strike extent in order to obtain the same observationally consistent seafloor and onshore displacements. Also shown is the source time function, specifically the potency rate per unit distance along strike. Our model underpredicts the duration of the earthquake, as compared with the inversion results of Yue and Lay (2011), but this is to be expected because our 2D simulations neglect later along-strike growth of the rupture. One difference between our model and the inversion results of Yue and Lay (2011) is the large initial increase in potency rate in our model due to the abrupt artificial nucleation procedure used, which contrasts with the more gradual onset of the earthquake inferred by Yue and Lay (2011).

Because effective normal stress is constant over the entire velocity-weakening portion of the fault, static stress drop is also relatively constant there. For this model, the average static stress drop between the seismogenic depth and the start of the velocity-strengthening region is 2.92 MPa. In the shallow velocity-strengthening region, there is a static stress increase of 0.75 MPa on average, or 4.2% of initial shear stress. This shallow portion of the fault does experience a dynamic stress drop of several MPa, with a maximum of 14 MPa approximately 5 km landward of the trench axis that results in a brief period of reverse slip; however, there is no permanent reversal of shear stress in the static field in this model. The near-trench dynamic stress drop is not caused by a drop in friction coefficient (because the fault is velocity-strengthening there), but is instead the result of a dynamic reduction in effective normal stress on the fault just landward of the trench. The large dynamic stress changes in the toe of the accretionary prism that we see in our model are likely moderated to some extent by inelastic deformation, which is neglected in our simulations. This issue deserves further attention.

We next turn to the seismic wave field. (Ⓔ Movies showing the evolution of the particle velocity field are available in the electronic supplement to this paper.) Figure 4 shows snapshots of the horizontal and vertical particle velocity fields at four times. Also shown are slip velocity and slip profiles. The first snapshot is 10 s after nucleation. The complexity of the fault geometry and material structure (Fig. 2) leads to a rich wave field. The hypocentral *P* and *S* waves

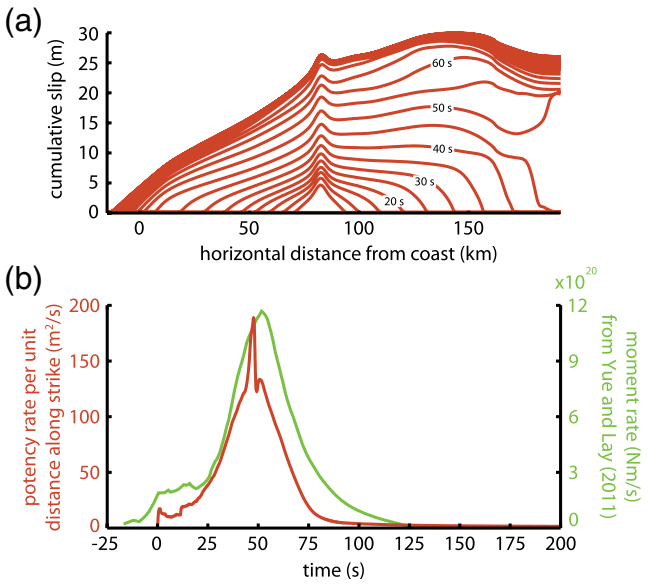

Figure 3. (a) Cumulative slip (plotted every 5 s) and (b) potency rate per unit distance along strike for our preferred dynamic rupture model. The latter is compared with the moment rate reported by Yue and Lay (2011). The moment rate from Yue and Lay (2011) has been time shifted −25 s to account for the abrupt nucleation procedure used in our dynamic rupture modeling. The color version of this figure is available only in the electronic edition.

have crossed through multiple material layers and reflected off the seafloor. These reflected waves, along with the bimaterial effect, lead to asymmetric expansion of the rupture. The low-velocity layers near the surface act as wave guides, leading to the development of dispersed wave trains. Similarly, the subducting plate channels waves along it.

The second snapshot (36 s) shows the rupture just before it enters the upper velocity-strengthening region. The largest particle velocities are in the fault normal direction, consistent with known solutions for subshear ruptures (e.g., Dunham and Archuleta, 2005). The velocities in the hanging wall are many times larger than those in the footwall, indicating that free-surface interactions are already significant. The next snapshot (48 s) is immediately after the rupture reaches the seafloor. Extreme horizontal motion in the toe of the accretionary prism is clearly visible. This is consistent with the amplification of ground motion in the hanging wall of thrust faults identified in previous studies (Brune, 1996; Oglesby *et al.*, 1998). The trapping and concentration of seismic waves within this thin sliver of material provides a driving force that enables vigorous rupture through the velocity-strengthening section of the fault up to the trench. The combination of large slip velocities and an extensive area of active sliding causes a peak in potency rate at this time, as shown in Figure 3. By this time, significant seafloor deformation has occurred. Fault slip continues in the form of a downward propagating rupture, as inferred by the seismic inversions of Ide *et al.* (2011), Yue and Lay (2011), and others, but in our model it dies out after several seconds. In other models we have conducted (Dunham and Kozdon, 2011; Kozdon and Dunham, 2011), this downgoing rupture propagates all the way to the bottom edge of the velocity-weakening seismogenic region.

The arrival of the rupture at the surface and the intensity of fault slip during this time strongly excite seismic waves. These breakout phases (Savage, 1965; Oglesby *et al.*, 1998; Madariaga, 2003) are shown in the final snapshot at 70 s. Most prominent is the dispersed Rayleigh-wave train propagating seaward, whose amplitude has been enhanced by forward directivity. The wave field in the landward direction is considerably more complex, particularly at high frequencies, due to interactions with the subducting plate.

With the goal of explaining features seen in onshore ground-motion data, we show several more snapshots of the wave field landward of the trench in Figure 5. The labels B–F indicate prominent arrivals on the horizontal component, and the corresponding letters with primes indicate these arrivals on the vertical component. The first snapshot (55 s) shows the wave field shortly after the rupture has broken through to the seafloor. The breakout phase begins with pulse B, which carries large seaward motions. This pulse becomes dispersed, as illustrated in the next snapshot (65 s), which shows multiple high-frequency reverberations in the low-velocity layers. The upper crustal layers channel energy along the seafloor, as seen in the third snapshot at 85 s. A similar packet of high-frequency waves is guided along the subducting plate.

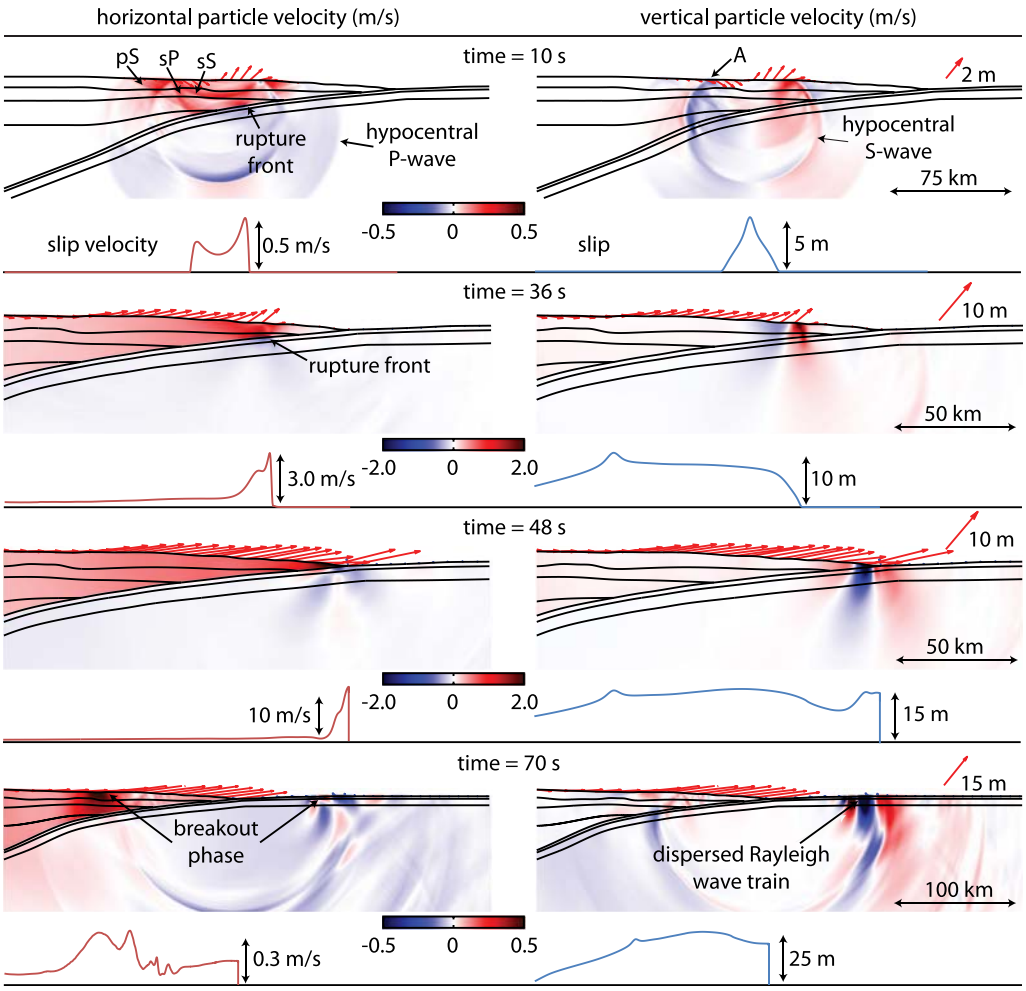

Figure 4. Snapshots of horizontal and vertical particle velocity. Length and (saturated) color scales vary between snapshots; no vertical exaggeration. The arrows on the free surface show seafloor deformation (the red and blue arrows are for points landward and seaward of the trench, respectively). Slip velocity and slip profiles (with horizontal distance aligned with the velocity field snapshots) are shown under the horizontal and vertical particle velocity fields, respectively. The color version of this figure is available only in the electronic edition.

Our model makes important predictions about surface displacement (at both seafloor and onshore locations) that can be compared with observations. We first present onshore ground-motion results. Figure 6 shows 1-Hz GPS data from GEONET station 0550 on the Oshika Peninsula, provided and processed by Shinichi Miyazaki (personal comm., April 2012). More details of the processing are given in Data and Resources. Also shown in Figure 6 are our model predictions at a point 215 km landward of the trench.

In addition to matching the overall trend and static displacements, our model captures several other features that are prominent in the data. This helps validate our model. Furthermore, because we have calculated the full wave field, it is straightforward to identify the origin of these features. To facilitate this comparison, we provide labels in Figure 6 that are identical to those in the wave-field snapshots of Figures 4 and 5. Note that the wave-field plots show particle velocity, while the ground motion is presented in terms of displacement.

Emergent deformation begins with the arrival of the hypocentral *P* wave, with displacement toward the trench and downward. Pulse A marks the arrival of the hypocentral *S* wave and closely arriving surface waves. The peak in displacement is enhanced by trapping of waves within the upper crustal layers. Simulations of rupture in a homogeneous medium (not shown) show a flatter displacement profile. This uplift is not seen in the data, which likely indicates that these phases are being enhanced in our model by the abrupt nucleation procedure we have employed. The following downward motion, between 45–55 s, is the fault normal velocity pulse propagating with, and slightly ahead of, a subshear rupture (e.g., Dunham and Archuleta, 2005). The slightly upward swing between 55–60 s is the fault normal velocity pulse of the opposite sign that trails the rupture. This is minimally expressed in our model because stopping phases from the cessation of slip at the lower edge of the seismogenic zone arrive at this time.

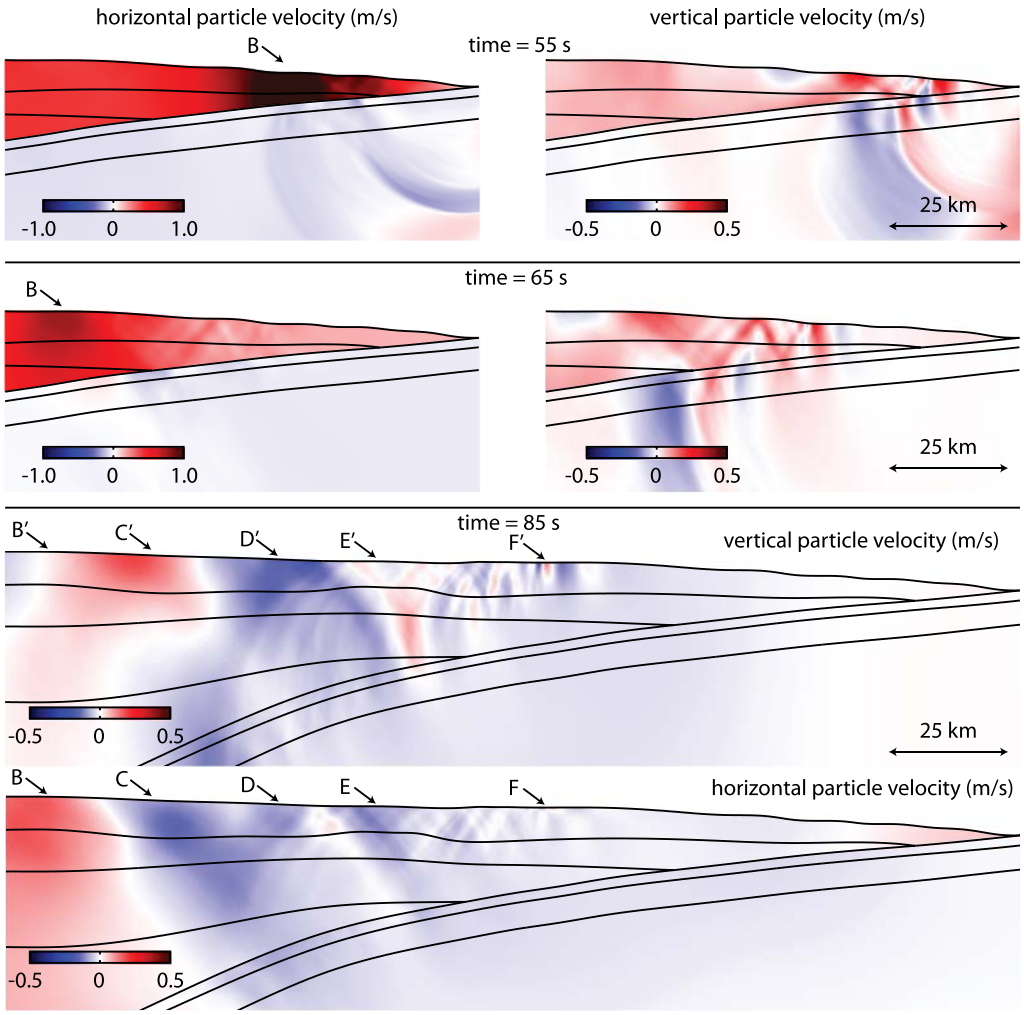

Figure 5. Snapshots of the wave field landward of the trench. Length scale of all the snapshots is the same, but the (saturated) color scale is different for the vertical and horizontal motion. Labels correspond to features seen in Figure 6, showing the surface deformation at 215 km from the trench. Explanations are given in the Dynamic Rupture Process section. The color version of this figure is available only in the electronic edition.

There are significant discrepancies between our model and the data in the horizontal component between 50–90 s. Many authors have described a more complex early rupture process than we have modeled, involving the failure of a deep asperity near the bottom edge of the seismogenic zone (Ide *et al.*, 2011). It is likely that adding heterogeneity in either frictional parameters or prestress would allow us to improve the waveform fit, as done by Goto *et al.* (2012), but that exercise runs counter to our main focus on the dynamics of the shallow plate interface and simple model parameterization.

The general trenchward and downward trend continues as the rupture propagates up the fault. When the rupture reaches the trench, it excites strong breakout phases. These arrive in pulses B–F. The initial long-period motions B–D exhibit prograde motion. This is similar to what is predicted by the analytical solution of Madariaga (2003) for rupture on a dipping fault in a uniform half-space. The later-arriving short-period motions (F) are dispersed Rayleigh waves trapped within the low-velocity crustal layers. This interpretation is confirmed by the retrograde particle motions. Overall, the correspondence between these waveform features in the data and our simulations provides compelling evidence for vigorous slip at the trench.

We also compare the final seafloor displacement in our model with observations (Fig. 7). Vertical seafloor uplift data nearest the trench come from ocean-bottom pressure gauges (Ito *et al.*, 2011). Horizontal displacements at these locations were obtained from acoustic ranging of a set of seafloor benchmarks; this technique has an error of ~20 m (Ito *et al.*, 2011). More accurate measurements using a combined GPS/acoustic ranging technique were made at a number of other sites farther from the trench (Kido *et al.*, 2011; Sato *et al.*, 2011). We also compare against data from the nearshore GPS station 1012 (Ozawa *et al.*, 2011). Because our model is 2D, we project the measurements onto a trench-perpendicular plane, thereby neglecting along-strike variations.

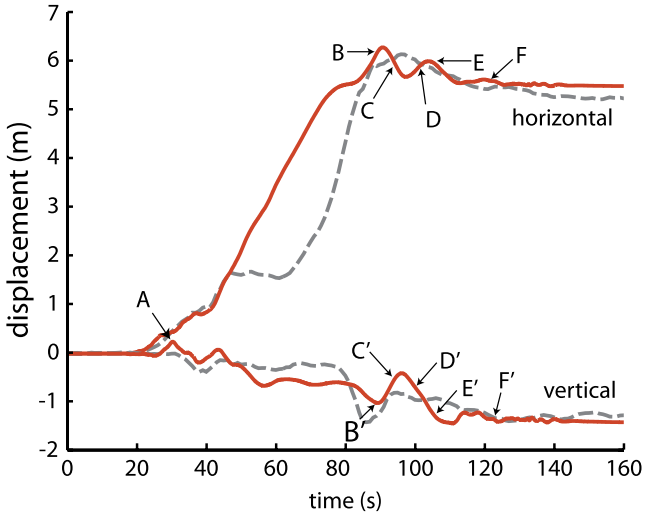

Figure 6. Comparison of the predicted horizontal and vertical surface deformation (solid line) at 215 km from the trench with 1-Hz GPS data (dashed line, provided by Shinichi Miyazaki, personal comm., April 2012). Labels identifying important features correspond to matching labels in the wave field shown in Figures 4 and 5. See the Dynamic Rupture Process section for explanation. The color version of this figure is available only in the electronic edition.

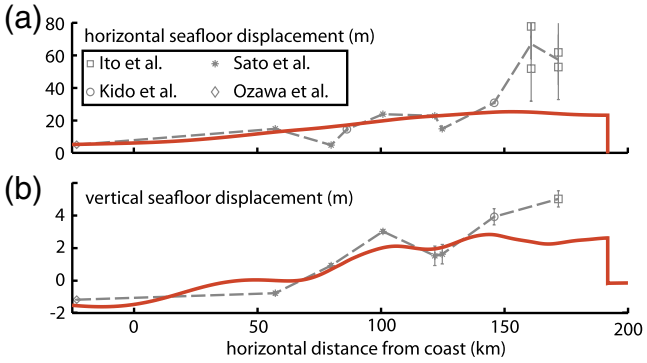

Figure 7. Horizontal and vertical seafloor deformation for our preferred model, compared with observations (dashed line); see the Dynamic Rupture Process section and Data and Resources. The data have been projected onto the trench-perpendicular plane; the error bars are those reported by the various authors. The color version of this figure is available only in the electronic edition.

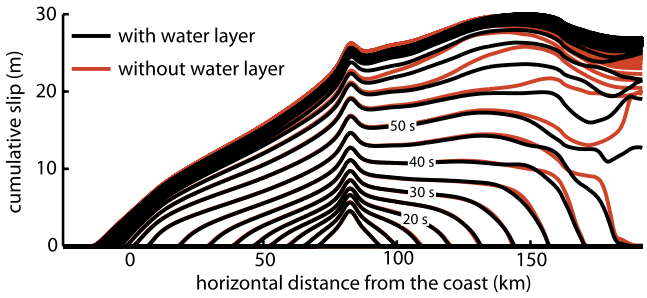

Figure 8. Cumulative slip (plotted every 5 s) for our preferred dynamic rupture model, both with and without a water layer. The color version of this figure is available only in the electronic edition.

With the exception of the horizontal displacement measurements nearest the trench (Ito *et al.*, 2011), which have large uncertainty, our preferred model matches the data well. We do underpredict the vertical displacement at the point closest to the trench, suggesting that actual slip at the trench may have been larger than in our model. Additionally, in the model the hinge line (which marks the transition between seafloor uplift and subsidence) is not as sharp as in the data. The location of the hinge line is largely related to deep slip and thus controlled by the seismogenic depth, as will be seen in the next section.

Sensitivity to Model Parameters

We arrived at our preferred model after conducting a parameter-space study to explore how certain model parameters and assumptions affect the rupture process. We first justify the neglect of the water layer and treatment of the seafloor as a free surface. To do this, we take parameters from our preferred model and add a water layer modeled as an isotropic linear acoustic material with a density of 1000 kg/m^3 and wave speed of 1.5 km/s. Figure 8 shows the cumulative slip for the preferred model both with and without the water layer. The two profiles are quite similar and differ on average between the trench axis and seismogenic depth by only 0.07%, with a maximum difference of 1 m near the trench axis.

We next turn to parameters along the fault. Foremost among these in controlling the rupture process are the initial effective normal stress, the horizontal width W of the shallow velocity-strengthening region (and its frictional properties), and the depth D of the seismogenic zone.

We first vary the frictional properties of the upper section of the fault under the accretionary prism. The width of this region is held fixed at $W = 30$ km, while we vary $b - a$. We consider three cases: velocity weakening ($b - a = 0.004$), neutrally stable ($b - a = 0$), and velocity strengthening ($b - a = -0.004$). Figure 9a compares the cumulative slip for the three cases, for maximum effective normal stress $\bar{\sigma}_{\max} = 40$ MPa and seismogenic depth $D = 45$ km. In all three cases rupture reaches the seafloor with large amounts of slip at the trench axis. The velocity-strengthening case does show a decrease in slip as the rupture enters the velocity-strengthening region, but this downward trend flattens as the rupture approaches the trench. This is caused by interactions with the free surface that enhance the shear loading from slip on the deeper, velocity-weakening portion of the fault. The relative amplitude of these shear-stress changes is exacerbated in the shallowest part of the fault where the initial effective normal stress becomes quite low.

In Figure 9b,c we present the predicted horizontal and vertical seafloor displacements, along with the seafloor deformation measurements discussed earlier (Ito *et al.*, 2011; Kido *et al.*, 2011; Ozawa *et al.*, 2011; Sato *et al.*, 2011). With the exception of the few measurements closest to the

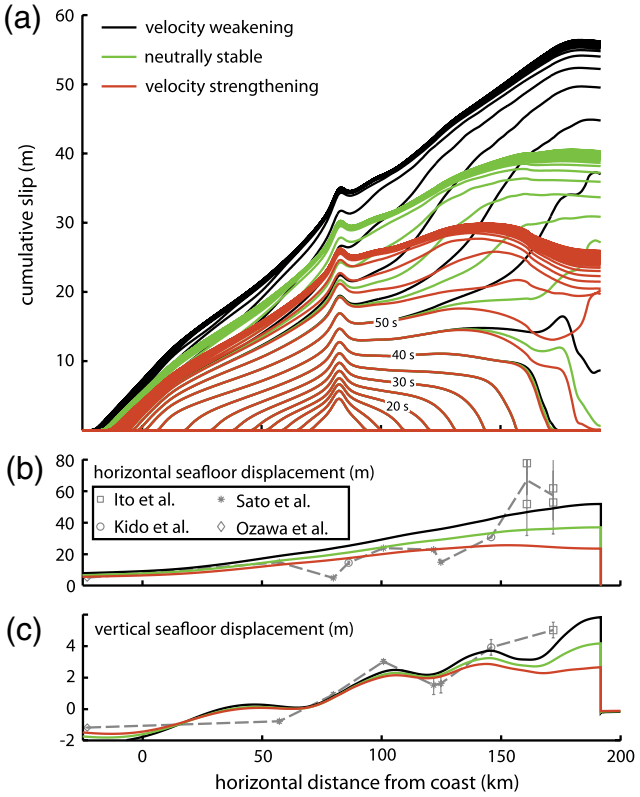

Figure 9. (a) Influence of frictional properties of the upper section of the fault (of horizontal width $W = 30$ km) on cumulative slip (plotted every 5 s). Shown for maximum effective normal stress $\bar{\sigma}_{\max} = 40$ MPa and seismogenic depth $D = 45$ km. (b) Horizontal and (c) vertical seafloor displacement compared with various observations (dashed line). The color version of this figure is available only in the electronic edition.

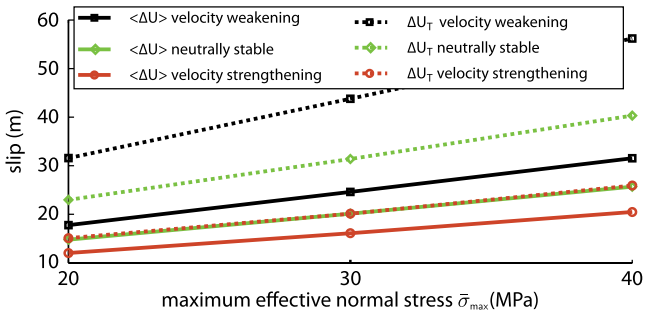

Figure 10. Influence of maximum effective normal stress $\bar{\sigma}_{\max}$ and frictional properties of the upper section of the fault (of horizontal width $W = 30$ km) on average slip $\langle \Delta u \rangle$ (solid lines) and slip at the trench Δu_T (dashed lines). Shown for seismogenic depth $D = 45$ km. The color version of this figure is available only in the electronic edition.

trench, the seafloor data are reasonably well fit by all models. The velocity-weakening model produces about 50% larger near-trench displacements compared with the velocity-strengthening case and better matches the few observations there. However, the waveform fit to the onshore 1-Hz GPS data (Fig. 6 for the velocity-strengthening case, not shown for velocity-weakening case) is quite poor for the velocity-weakening case. This misfit is partially evident in the static deformation field at the coast, as shown in Figure 9b,c.

Changing effective normal stress (and, thus, stress drop) has little effect on the overall solution structure and largely acts as a scaling parameter. To demonstrate this, we compare average slip, $\langle \Delta u \rangle$, and slip at the trench, Δu_T, for $\bar{\sigma}_{\max} =$ 20, 30, and 40 MPa in Figure 10. Average slip is calculated over parts of the fault experiencing slip greater than the state-evolution distance L. Both trench slip and average slip scale almost linearly with $\bar{\sigma}_{\max}$. The ratio of trench slip to average slip for the three cases is 1.8 for the velocity-weakening case, 1.6 for the neutrally stable case, and 1.3 for the velocity-strengthening case. A ratio of two is predicted for a triangular-shaped slip distribution that increases linearly from zero to Δu_T along the fault.

In all simulations thus far we have assumed that the horizontal extent of shallow region with altered frictional properties is $W = 30$ km. Changing this will clearly have an impact on the slip and seafloor deformation. Figure 11 compares slip distributions for velocity-strengthening regions of various W (with $\bar{\sigma}_{\max} = 40$ MPa and $D = 45$ km). The $W = 0$ case, corresponding to velocity-weakening friction all the way to the trench, is shown in Figure 9a. For our specific parameter choices, ruptures will reach the trench for W less than about 55 km. When rupture does reach the trench, free-surface interactions significantly enhance slip, despite the velocity-strengthening nature of the fault in this region.

Figure 11b,c shows horizontal and vertical seafloor deformation, respectively. In the case of the surface-breaking ruptures, the horizontal and vertical seafloor deformation is large at the trench. The hinge line is moved slightly landward by increasing W, though (as will be seen) changes are negligible compared with those caused by changing the downdip extent of slip through the seismogenic depth D. Figure 12 compares the average slip $\langle \Delta u \rangle$ and slip at the trench Δu_T for both the velocity-strengthening and neutrally stable cases with various values of W. Slip at the trench decreases linearly until $W \approx 52$ km, after which point there is an abrupt drop in slip at the trench until it reaches zero at $W \approx 55$ km. This propensity for increasingly unstable slip as ruptures approach the free surface has been discussed by Dmowska and Rice (1986) and Rudnicki and Wu (1995).

The final parameter of interest is the depth extent of the seismogenic zone D, which we have thus far held fixed at $D = 45$ km. Figure 13a shows the cumulative slip for $D = 30$, 45, and 60 km for the velocity-strengthening case with $\bar{\sigma}_{\max} = 40$ MPa and $W = 30$ km. Slip decreases as D decreases, as expected when the crack length is reduced. However, the basic character of the slip profile is the same. As illustrated in Figure 14, the effect of D on average slip and trench slip is minimal compared with the effect of $\bar{\sigma}_{\max}$ or W. The more striking change is in the seafloor deformation, as shown in Figure 13b,c. The hinge line is moved toward the

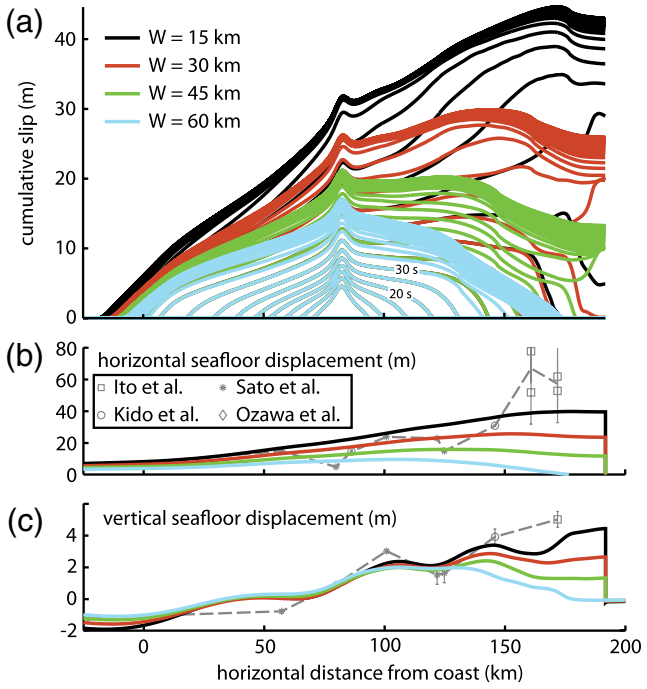

Figure 11. (a) Influence of horizontal extent W of shallow velocity-strengthening region on cumulative slip (plotted every 5 s). Shown for maximum effective normal stress $\bar{\sigma}_{\max} = 40$ MPa and seismogenic depth $D = 45$ km. (b) Horizontal and (c) vertical seafloor displacement compared with various observations (dashed line). The color version of this figure is available only in the electronic edition.

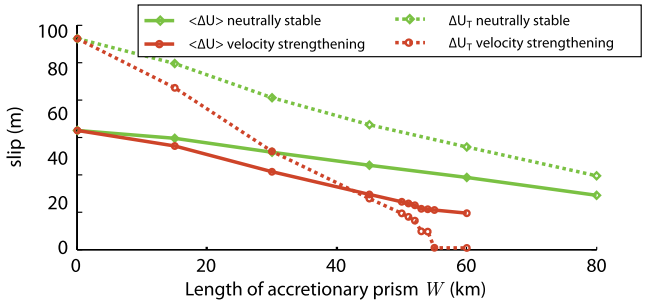

Figure 12. Influence of horizontal extent W of shallow velocity-strengthening or neutrally stable region on average slip $\langle \Delta u \rangle$ (solid lines) and slip at the trench Δu_T (dashed lines). Shown for maximum effective normal stress $\bar{\sigma}_{\max} = 40$ MPa and seismogenic depth $D = 45$ km. The color version of this figure is available only in the electronic edition.

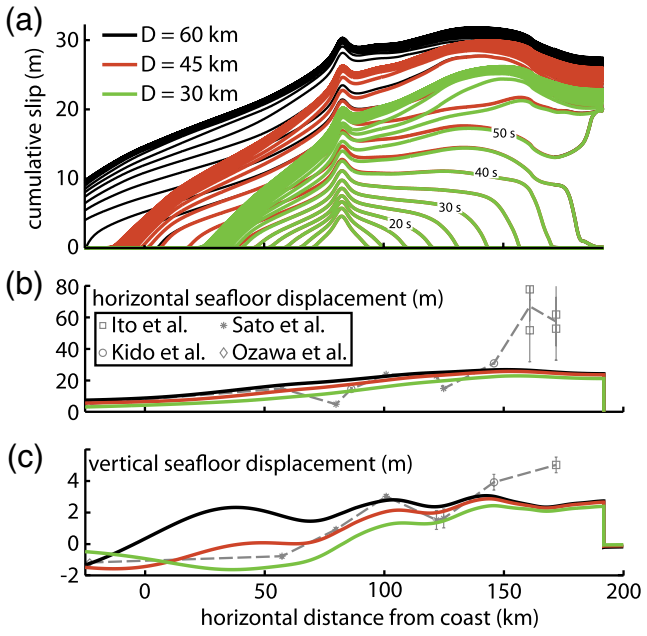

Figure 13. (a) Influence of seismogenic depth D on cumulative slip (plotted every 5 s), shown for velocity-strengthening upper fault ($W = 30$ km) and maximum effective normal stress $\bar{\sigma}_{\max} = 40$ MPa. (b) Horizontal and (c) vertical seafloor displacement compared with various observations (dashed line). The color version of this figure is available only in the electronic edition.

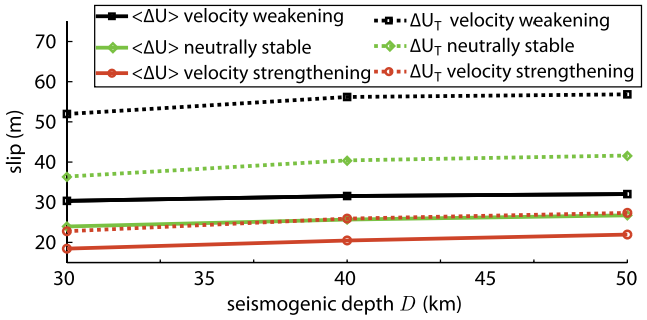

Figure 14. Influence of seismogenic depth D on average slip $\langle \Delta u \rangle$ (solid lines) and slip at the trench Δu_T (dashed lines), shown for various frictional properties along the upper part of the fault ($W = 30$ km) and maximum effective normal stress $\bar{\sigma}_{\max} = 40$ MPa. The color version of this figure is available only in the electronic edition.

trench with decreasing D, and the shape of the vertical deformation is changed. In addition, we find that the onshore 1-Hz GPS data fits are quite sensitive to D. Based on these comparisons, we selected $D = 45$ km for our preferred model.

An important outcome of the parameter-space study is that frictional parameters beneath the accretionary wedge and the maximum effective normal stress (which controls average stress drop) cannot be determined independently based on the data employed in this study. This is demonstrated in Figure 15, which shows the slip, static seafloor displacement, and onshore displacement waveforms for the velocity-strengthening model with $\bar{\sigma}_{\max} = 40$ MPa, the neutrally stable model with $\bar{\sigma}_{\max} = 30$ MPa, and the velocity-weakening model with $\bar{\sigma}_{\max} = 25$ MPa; for all three models $D = 45$ km and $W = 30$ km. Away from the trench the slip profiles are quite similar, as are the static seafloor displacements. Near the trench, the three models exhibit pronounced differences in slip, but the influence on seafloor deformation

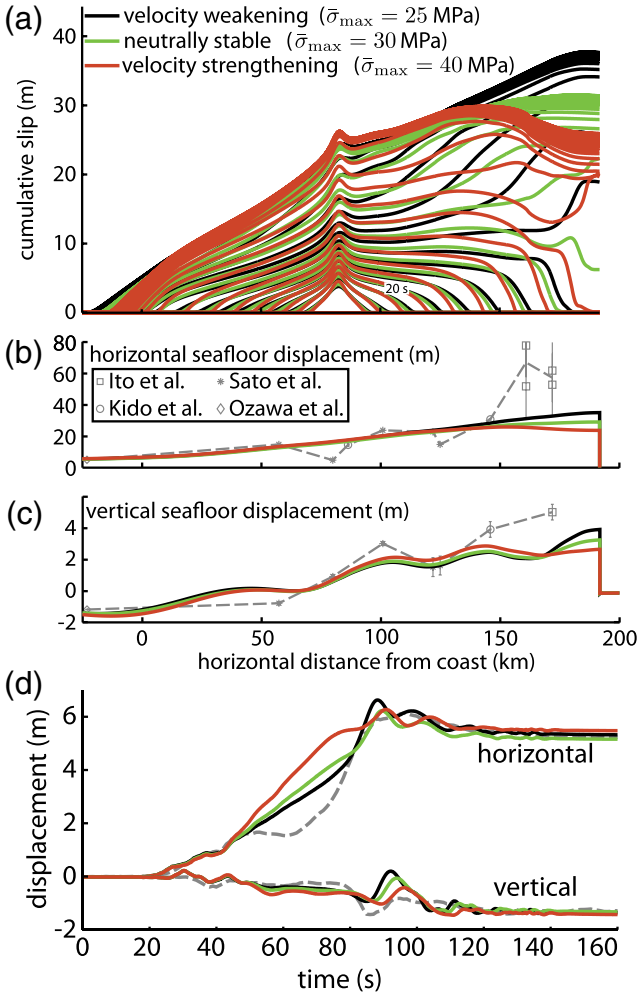

Figure 15. (a) Influence of maximum effective normal stress $\bar{\sigma}_{\max}$ on cumulative slip for the velocity-weakening, neutrally stable, and velocity-strengthening models ($W = 30$ km and $D = 45$ km for all models). (b) Horizontal and (c) vertical seafloor displacement compared with various observations (dashed line). (d) Comparison of the predicted horizontal and vertical surface deformation from the three models (solid lines) at 215 km from the trench with 1-Hz GPS data (dashed line). The color version of this figure is available only in the electronic edition.

and the onshore displacement waveforms is remarkably minimal. This demonstrates that the near-trench fault properties are, unfortunately, not well constrained by the data.

Discussion

Using dynamic rupture simulations of the Tohoku earthquake, we have explored the ability of ruptures to reach the trench in megathrust earthquakes, even when the uppermost segment of the plate interface is velocity strengthening. In addition to rigorously solving rate-and-state friction (instead of approximating this with a slip-weakening law), we account for realistic depth-dependent material structure and the complex geometry of the fault, seafloor, and material layer interfaces. All of these are essential to explain various features of the static seafloor deformation and dynamic onshore displacements.

We find that stress changes from slip on the deeper, velocity-weakening section of the fault easily drive ruptures through velocity-strengthening segments up to 55 km long. While this specific limit may be sensitive to the choice of frictional properties and the geometry of the subduction zone, our simulations do show that it is unnecessary to invoke extreme dynamic weakening mechanisms (such as thermal pressurization) or shallow asperities having large stress drops (from subduction of seamounts, for example) to explain the large slip near the trench. That being said, we do not argue against the possibility of extreme weakening and large stress drop near the trench. In fact, those processes would likely improve the fit to seafloor deformation data in the near-trench region, and investigating them should be a high priority.

We tested the robustness of our results and characterized their sensitivity to model parameters by conducting a set of simulations varying effective normal stress (and, therefore, stress drop), width of the shallow frictionally stable fault segment, and seismogenic depth. Model predictions were compared with measurements of seafloor deformation and the time history of onshore displacements recorded at a 1-Hz GPS station. This parameter study indicated that the effective normal stress is largely a scaling parameter controlling the overall amount of slip by varying the stress drop. Our preferred model has an average static stress drop of 2.92 MPa in the velocity-weakening region and an average static stress increase of 0.75 MPa in the shallow velocity-strengthening region. The downdip limit of the seismogenic zone was found to be the strongest controlling factor in determining the hinge line location of seafloor deformation.

Perhaps the most substantial approximation we have made is neglecting inelastic deformation of the accretionary prism. Our simulations, which assume ideally elastic material response everywhere off the fault, predict massive static and dynamic stress changes in the toe of the prism, including a transient reversal in the sense of shear stress and slip. Plastic deformation of the wedge would provide an additional energy sink that would make it more difficult for ruptures to break through to the seafloor and might prevent the stress reversal. We speculate that plasticity in the accretionary prism could be responsible for preventing rupture to the trench in other megathrust earthquakes, such as the 2005 Nias–Simeulue event (Hsu *et al.*, 2006). Future work, such as the dynamic rupture simulations by Ma (2012) for planar dipping faults in uniform half-spaces, will hopefully shed light on this issue.

Our simulations make specific predictions about what might be observed during IODP Expedition 343: Japan Trench Fast Drilling Project (JFAST) (Mori *et al.*, 2012), which drilled across the fault a few kilometers landward of the trench. One of the goals of JFAST is to identify a temperature anomaly around the slip zone that can be used to constrain the shear stress on the fault during active sliding.

With this in mind, we calculated the energy per unit fault area dissipated by frictional sliding, at locations 800–900 meters below sea level, corresponding to the JFAST target sites. Specifically, we integrated the work rate τV over time, obtaining values around 190 MJ/m^2. A close examination of the time histories of τ and V at these locations reveals that shear stress surprisingly remains relatively constant during sliding and is reduced (through reduction in effective normal stress) only after most slip has accumulated, presumably by stress transfer from deeper slip. The dissipated energy per area can thus be approximated as the product of the total slip (26 m at this location) and an average coseismic shear stress of 7 MPa. The latter is simply the product of the initial effective normal stress (about 12 MPa) and the friction coefficient (roughly equal to the reference friction coefficient $f_0 = 0.6$).

It is possible that models with much lower τ during sliding, either through a lower f_0 along this uppermost section of the fault or through the onset of dynamic weakening, might equally well match the ground-motion and deformation data used in this study, but we did not explore that possibility in these simulations.

We close with a brief discussion concerning hydroacoustic waves excited by megathrust earthquakes. As mentioned previously, the effect of the water layer on the rupture process is minimal (Fig. 8). That said, inclusion of the water layer does allow us to make direct comparisons with ocean-bottom pressure measurements of the sort presented by Maeda *et al.* (2011), which show both hydroacoustic waves and later-arriving surface gravity waves (tsunamis). Our free-surface boundary condition is enforced on the unperturbed sea surface, preventing us from modeling surface gravity waves, but this approximation does little to compromise the accuracy of hydroacoustic wave propagation and reflection from the sea surface. In Figure 16 we show the vertical particle velocity for our preferred model with a water layer (compare with Figs. 4 and 5). (Ⓔ Movies showing the evolution of the particle velocity field are available in the electronic supplement to this paper.) Figure 16 also shows the seafloor pressure history at a few sites landward of the trench. In addition to reverberations excited by hypocentral seismic waves (which are likely overly pronounced due to our nucleation procedure), there are prominent hydroacoustic arrivals excited when the rupture reaches the trench. Though it is beyond the scope of this paper, these signals, which are the direct result of dynamic seafloor deformation, may contain invaluable information that could be used in local tsunami early warning systems and should be explored further.

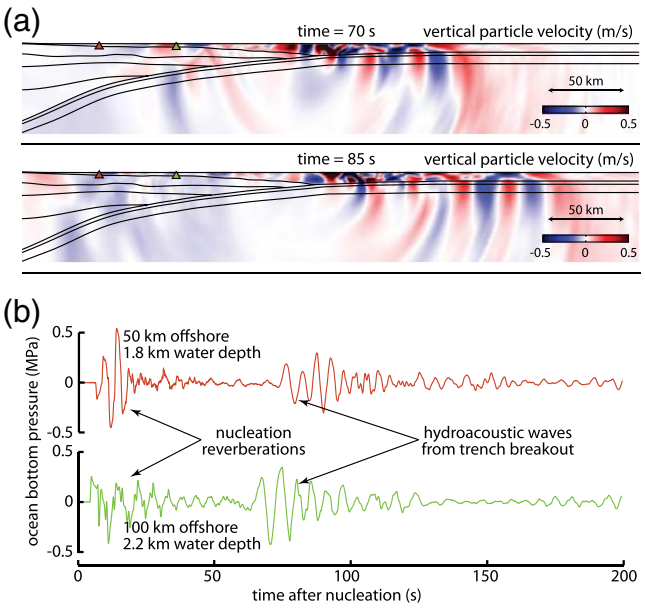

Figure 16. (a) Vertical particle velocity wave-field snapshots for our preferred model with a water layer (modeled as an isotropic linear acoustic medium). (b) Pressure changes from hydroacoustic waves at seafloor locations indicated by triangles in (a). The color version of this figure is available only in the electronic edition.

Data and Resources

The numerical simulations were conducted at the Stanford Center for Computational Earth and Environmental Science (CEES). Seafloor deformation data were compiled from Ito *et al.* (2011), Kido *et al.* (2011), and Sato *et al.* (2011). Nearshore GPS data were taken from Ozawa *et al.* (2011) (station number 1012). The geometry, velocity, and density structure were derived from figures of Miura *et al.* (2001, 2005). The onshore 1-Hz GPS data (station number 0550 of GEONET operated by the Geospatial Information Authority of Japan) were provided by Shinichi Miyazaki (personal comm., April 2012), who purchased the original RINEX data from Nippon GPS Data Service Corporation and processed them using the precise point positioning strategy with phase ambiguities resolved using GIPSY-OASIS software (Zumberge *et al.*, 1997); station position errors were modeled as a white noise process.

Acknowledgments

JEK was supported by the NSF Fellowship for Transformative Computational Science using CyberInfrastructure OCI-1122734. We thank Emily Brodsky for inspiring this work by her request for Tohoku simulations in support of the JFAST proposal. Discussions with Paul Segall, Greg Beroza, Shinichi Miyazaki, and Satoshi Ide were invaluable.

References

Brune, J. N. (1996). Particle motions in a physical model of shallow angle thrust faulting, *Proc. Indian Acad. Sci.* **105,** no. 2, 197–206, doi: 10.1007/BF02876014.

Byrne, D., D. M. Davis, and L. R. Sykes (1988). Loci and maximum size of thrust earthquakes and the mechanics of the shallow region of subduction zones, *Tectonics* **7,** no. 4, 833–857, doi: 10.1029/TC007i004p00833.

Carpenter, M. H., D. Gottlieb, and S. Abarbanel (1994). Time-stable boundary conditions for finite-difference schemes solving hyperbolic systems: Methodology and application to high-order compact schemes, *J. Comp. Phys.* **111,** no. 2, 220–236, doi: 10.1006/jcph.1994.1057.

Cocco, M., and J. R. Rice (2002). Pore pressure and poroelasticity effects in Coulomb stress analysis of earthquake interactions, *J. Geophys. Res.* **107,** no. B2, 2030, doi: 10.1029/2000JB000138.

Cochard, A., and J. R. Rice (2000). Fault rupture between dissimilar materials: Ill-posedness, regularization and slip-pulse response, *J. Geophys. Res.* **105,** no. B11, 25,891–25,907, doi: 10.1029/2000JB900230.

den Hartog, S. A., C. J. Peach, D. M. de Winter, C. J. Spiers, and T. Shimamoto (2012). Frictional properties of megathrust fault gouges at low sliding velocities: New data on effects of normal stress and temperature, *J. Struct. Geol.* **38**, 156–171, doi: 10.1016/j.jsg.2011.12.001.

Dmowska, R., and B. V. Kostrov (1973). A shearing crack in a half-space under plane strain conditions, *Arch. Mech.* **25,** no. 3, 421–440.

Dmowska, R., and J. R. Rice (1986). Fracture theory and its seismological applications, in *Continuum Theories in Solid Earth Physics*, PWN-Polish Scientific Publishers, Warsaw, Poland, 187–225.

Duan, B. (2012). Dynamic rupture of the 2011 M_w 9.0 Tohoku-Oki earthquake: Roles of a possible subducting seamount, *J. Geophys. Res.* **117,** B05311, doi: 10.1029/2011JB009124.

Dunham, E. M., and R. J. Archuleta (2005). Near-source ground motion from steady state dynamic rupture pulses, *Geophys. Res. Lett.* **32,** L03302, doi: 10.1029/2004GL021793.

Dunham, E. M., and J. E. Kozdon (2011). Rupture dynamics of subduction megathrust earthquakes, Abstract T31E-05 presented at 2011 Fall Meeting, AGU, San Francisco, California, 5–9 December 2011.

Dunham, E. M., and J. R. Rice (2008). Earthquake slip between dissimilar poroelastic materials, *J. Geophys. Res.* **113,** B09304, doi: 10.1029/2007JB005405.

Eshelby, J. D. (1969). The elastic field of a crack extending non-uniformly under general anti-plane loading, *J. Mech. Phys. Solids* **17,** no. 3, 177–199, doi: 10.1016/0022-5096(69)90032-5.

Faulkner, D. R., T. M. Mitchell, J. Behnsen, T. Hirose, and T. Shimamoto (2011). Stuck in the mud? Earthquake nucleation and propagation through accretionary forearcs, *Geophys. Res. Lett.* **38,** L18303, doi: 10.1029/2011GL048552.

Fossum, A. F., and L. B. Freund (1975). Nonuniformly moving shear crack model of a shallow focus earthquake mechanism, *J. Geophys. Res.* **80,** no. 23, 3343–3347, doi: 10.1029/JB080i023p03343.

Fujiwara, T., S. Kodaira, T. No, Y. Kaiho, N. Takahashi, and Y. Kaneda (2011). The 2011 Tohoku-Oki earthquake: Displacement reaching the trench axis, *Science* **334,** no. 6060, doi: 10.1126/science.1211554.

Goto, H., Y. Yamamoto, and S. Kita (2012). Dynamic rupture simulation of the 2011 off the Pacific coast of Tohoku earthquake: Multi-event generation within dozens of seconds, *Earth Planets Space*, 1–9, doi: 10.5047/eps.2012.06.002.

Hsu, Y., M. Simons, J. Avouac, J. Galetzka, K. Sieh, M. Chlieh, D. Natawidjaja, L. Prawirodirdjo, and Y. Bock (2006). Frictional afterslip following the 2005 Nias–Simeulue earthquake, Sumatra, *Science* **312,** no. 5782, 1921–1926, doi: 10.1126/science.1126960.

Hyndman, R. D., M. Yamano, and D. A. Oleskevich (1997). The seismogenic zone of subduction thrust faults, *Island Arc* **6,** no. 3, 244–260, doi: 10.1111/j.1440-1738.1997.tb00175.x.

Ide, S., A. Baltay, and G. C. Beroza (2011). Shallow dynamic overshoot and energetic deep rupture in the 2011 M_w 9.0 Tohoku-Oki earthquake, *Science* **332,** no. 6036, 1426–1429, doi: 10.1126/science.1207020.

Ikari, M. J., D. M. Saffer, and C. Marone (2009). Frictional and hydrologic properties of clay-rich fault gouge, *J. Geophys. Res.* **114,** B05409, doi: 10.1029/2008JB006089.

Ito, Y., T. Tsuji, Y. Osada, M. Kido, D. Inazu, Y. Hayashi, H. Tsushima, R. Hino, and H. Fujimoto (2011). Frontal wedge deformation near the source region of the 2011 Tohoku-Oki earthquake, *Geophys. Res. Lett.* **38,** L00G05, doi: 10.1029/2011GL048355.

Kennett, B. L. N., A. Gorbatov, and E. Kiser (2011). Structural controls on the M_w 9.0 2011 offshore-Tohoku earthquake, *Earth Planet Sci. Lett.* **310,** no. 3–4, 462–467, doi: 10.1016/j.epsl.2011.08.039.

Kido, M., Y. Osada, H. Fujimoto, R. Hino, and Y. Ito (2011). Trench-normal variation in observed seafloor displacements associated with the 2011 Tohoku-Oki earthquake, *Geophys. Res. Lett.* **38,** L24303, doi: 10.1029/2011GL050057.

Kodaira, S., T. No, Y. Nakamura, T. Fujiwara, Y. Kaiho, S. Miura, N. Takahashi, Y. Kaneda, and A. Taira (2012). Coseismic fault rupture at the trench axis during the 2011 Tohoku-oki earthquake, *Nature Geosci.* **5,** no. 9, 646–650, doi: 10.1038/ngeo1547.

Kozdon, J. E., and E. M. Dunham (2011). Rupture to the trench in dynamic models of the Tohoku-Oki earthquake, Abstract U51B-0041 presented at 2011 Fall Meeting, AGU, San Francisco, California, 5–9 December 2011.

Kozdon, J. E., E. M. Dunham, and J. Nordström (2012). Simulation of dynamic earthquake ruptures in complex geometries using high-order finite difference methods, *J. Sci. Comp*, in press, doi: 10.1007/s10915-012-9624-5.

Kreiss, H., and G. Scherer (1974). Finite element and finite difference methods for hyperbolic partial differential equations, in *Mathematical aspects of finite elements in partial differential equations; Proceedings of the Symposium*, Madison, Wisconsin, 195–212.

Lapusta, N., J. R. Rice, Y. Ben-Zion, and G. Zheng (2000). Elastodynamic analysis for slow tectonic loading with spontaneous rupture episodes on faults with rate- and state-dependent friction, *J. Geophys. Res.* **105,** 23,765–23,789, doi: 10.1029/2000JB900250.

Ma, S. (2012). A self-consistent mechanism for slow dynamic deformation and tsunami generation for earthquakes in the shallow subduction zone, *Geophys. Res. Lett.* **39,** no. 11, doi: 10.1029/2012GL051854.

Madariaga, R. (2003). Radiation from a finite reverse fault in a half space, *Pure. Appl. Geophys.* **160,** no. 3–4, 555–577, doi: 10.1007/PL00012550.

Maeda, T., T. Furumura, S. Sakai, and M. Shinohara (2011). Significant tsunami observed at ocean-bottom pressure gauges during the 2011 off the Pacific coast of Tohoku earthquake, *Earth Planets Space* **63,** 803–808, doi: 10.5047/eps.2011.06.005.

Marone, C., and C. H. Scholtz (1988). The depth of seismic faulting and the upper transition from stable to unstable slip regimes, *Geophys. Res. Lett.* **15,** no. 6, 621–624, doi: 10.1029/GL015i006p00621.

Matsubara, M., and K. Obara (2011). The 2011 off the Pacific coast of Tohoku earthquake related to a strong velocity gradient with the Pacific plate, *Earth Planets Space* **63,** 663–667, doi: 10.5047/eps.2011.05.018.

Mitsui, Y., N. Kato, Y. Fukahata, and K. Hirahara (2012). Megaquake cycle at the Tohoku subduction zone with thermal fluid pressurization near the surface, *Earth Planet. Sci. Lett.* **325,** 21–26, doi: 10.1016/j.epsl.2012.01.026.

Miura, S., N. Takahashi, A. Nakanishi, A. Ito, S. Kodaira, T. Tsuru, and Y. Kaneda (2001). Seismic velocity structure off Miyagi fore-arc region, Japan Trench, using ocean bottom seismographic data, *Frontier Res. Earth Evolut.* **1,** 337–340.

Miura, S., N. Takahashi, A. Nakanishi, T. Tsuru, S. Kodaira, and Y. Kaneda (2005). Structural characteristics off Miyagi forearc region, the Japan Trench seismogenic zone, deduced from a wide-angle reflection and refraction study, *Tectonophys* **407,** no. 3–4, 165–188, doi: 10.1016/j.tecto.2005.08.001.

Moore, J. C., and D. Saffer (2001). Updip limit of the seismogenic zone beneath the accretionary prism of southwest Japan: An effect of diagenetic to low-grade metamorphic processes and increasing effective stress, *Geology* **29,** no. 2, 183–186, doi: 10.1130/0091-7613(2001)029<0183:ULOTSZ>2.0.CO;2.

Mori, J., F. M. Chester, N. Eguchi, and S. Toczko (2012). Japan Trench Fast Earthquake Drilling Project (JFAST), *IODP Sci. Prosp.* **343,** doi: 10.2204/iodp.sp.343.2012.

Noda, H., and N. Lapusta (2011). Rich fault behavior due to combined effect of rate strengthening friction at low slip rates and coseismic weakening: Implications for Chi-Chi and Tohoku earthquakes, Abstract T42C-03 presented at 2011 Fall Meeting, AGU, San Francisco, California, 5–9 December 2011.

Oglesby, D. D., R. J. Archuleta, and S. B. Nielsen (1998). Earthquakes on dipping faults: The effects of broken symmetry, *Science* **280,** no. 5366, 1055–1059, doi: 10.1126/science.280.5366.1055.

Ozawa, S., T. Nishimura, H. Suito, T. Kobayashi, M. Tobita, and T. Imakiire (2011). Coseismic and postseismic slip of the 2011 magnitude-9 Tohoku-Oki earthquake, *Nature* **475,** 373–376, doi: 10.1038/nature10227.

Prakash, V. (1998). Frictional response of sliding interfaces subjected to time varying normal pressures, *J. Tribol.* **120,** no. 1, 97–102, doi: 10.1115/1.2834197.

Prakash, V., and R. J. Clifton (1993). Time resolved dynamic friction measurements in pressure-shear, in *Experimental Techniques in the Dynamics of Deformable Solids*, A. K. T. Ramesh (Editor), Appl. Mech. Div., ASME, New York, 33–48.

Ranjith, K., and J. R. Rice (2001). Slip dynamics at an interface between dissimilar materials, *J. Mech. Phys. Solids* **49,** no. 2, 341–361, doi: 10.1016/S0022-5096(00)00029-6.

Rice, J. R. (1992). Fault stress states, pore pressure distributions, and the weakness of the San Andreas fault, in *Fault Mechanics and Transport Properties in Rocks*, edited by B. Evans and T.-F. Wong, Academic Press, London, United Kingdom, 475–503.

Rice, J. R., and M. P. Cleary (1976). Some basic stress diffusion solutions for fluid-saturated elastic porous media with compressible constituents, *Rev. Geophys. Space Phys.* **14,** no. 2, 227–241, doi: 10.1029/RG014i002p00227.

Rice, J. R., N. Lapusta, and K. Ranjith (2001). Rate and state dependent friction and the stability of sliding between elastically deformable solids, *J. Mech. Phys. Solids* **49,** no. 9, 1865–1898, doi: 10.1016/S0022-5096(01)00042-4

Rudnicki, J. W., and J. R. Rice (2006). Effective normal stress alteration due to pore pressure changes induced by dynamic slip propagation on a plane between dissimilar materials, *J. Geophys. Res.* **111,** B10308, doi: 10.1029/2006JB004396.

Rudnicki, J. W., and M. Wu (1995). Mechanics of dip-slip faulting in an elastic half-space, *J. Geophys. Res.* **100,** no. B11, 22,173–22,186, doi: 10.1029/95JB02246.

Saffer, D. M., and C. Marone (2003). Comparison of smectite- and illite-rich gouge frictional properties: Application to the updip limit of the seismogenic zone along subduction megathrusts, *Earth Planet. Sci. Lett.* **215,** no. 1–2, 219–235, doi: 10.1016/S0012-821X(03)00424-2.

Saffer, D. M., and H. J. Tobin (2011). Hydrogeology and mechanics of subduction zone forearcs: Fluid flow and pore pressure, *Annu. Rev. Earth Planet. Sci.* **39,** 157–186, doi: 10.1146/annurev-earth-040610-133408.

Sato, M., T. Ishikawa, N. Ujihara, S. Yoshida, M. Fujita, M. Mochizuki, and A. Asada (2011). Displacement above the hypocenter of the 2011 Tohoku-Oki earthquake, *Science* **332,** no. 6036, doi: 10.1126/science.1207401.

Savage, J. C. (1965). The stopping phase on seismograms, *Bull. Seismol. Soc. Am.* **55,** no. 1, 47–58.

Shibazaki, B., T. Matsuzawa, A. Tsutsumi, K. Ujiie, A. Hasegawa, and Y. Ito (2011). 3D modeling of the cycle of a great Tohoku-Oki earthquake, considering frictional behavior at low to high slip velocities, *Geophys. Res. Lett.* **38,** L21305, doi: 10.1029/2011GL049308.

Strand, B. (1994). Summation by parts for finite difference approximations for d/dx, *J. Comp. Phys.* **110,** no. 1, 47–67, doi: 10.1006/jcph.1994.1005.

Ujiie, K., and A. Tsutsumi (2010). High-velocity frictional properties of clay-rich fault gouge in a megasplay fault zone, Nankai subduction zone, *Geophys. Res. Lett.* **37,** L24310, doi: 10.1029/2010GL046002.

Wang, H. F. (2000). *Theory of Linear Poroelasticity with Applications to Geomechanics and Hydrogeology*, Princeton University Press, Princeton, New Jersey.

Vrolijk, P. (1990). On the mechanical role of smectite in subduction zones, *Geol.* **18,** no. 8, 703–707, doi: 10.1130/0091-7613(1990)018<0703:OTMROS>2.3.CO;2.

Yue, H., and T. Lay (2011). Inversion of high-rate (1 sps) GPS data for rupture process of the 11 March 2011 Tohoku earthquake (M_w 9.1), *Geophys. Res. Lett.* **38,** L00G09, doi: 10.1029/2011GL048700.

Zumberge, J. F., M. B. Heflin, D. C. Jefferson, M. M. Watkins, and F. H. Webb (1997). Precise point positioning for the efficient and robust analysis of GPS data from large networks, *J. Geophys. Res.* **102,** no. B3, 5005–5017, doi: 10.1029/96JB03860.

Department of Geophysics
Stanford University
397 Panama Mall
Stanford, California 94305
jekozdon@nps.edu
(J.E.K.)

Department of Geophysics and Institute for Computational and Mathematical Engineering
Stanford University
397 Panama Mall
Stanford, California 94305
edunham@stanford.edu
(E.M.D.)

Manuscript received 9 April 2012